Prediction of biopore and matrix dominated flow from X-ray CT-derived macropore network characteristics

Muhammad Naveed[1], Per Moldrup[3], Marcel Schaap[4], Markus Tuller[4], Ramaprasad Kulkarni[4,5], Hans-Jörg Vogel[6], and Lis Wollesen de Jonge[2]*

[1]Institute of Biological and Environmental Sciences, University of Aberdeen, King's College, Aberdeen AB24 3FX, United Kingdom.

[2]Department of Agroecology, Faculty of Science and Technology, Aarhus University, Blichers Allé 20, Postbox 50, DK-8830 Tjele, Denmark.

[3]Department of Civil Engineering, Aalborg University, Sohngaardsholmsvej 57, DK-9000 Aalborg, Denmark.

[4]Department of Soil, Water and Environmental Science, The University of Arizona, 1177 E. 4th Street, Tucson, AZ 85721, United States.

[5]Department of Electrical and Computer Engineering, The University of Arizona, 1230 E Speedway Blvd., Tucson, AZ 85721, United States.

[6]Department of Soil Physics, Helmholtz Center for Environmental Research-UFZ, Theodor-Lieser-Straße 4, 06120 Halle [Saale], Germany.

***Corresponding Author:**

Muhammad Naveed

Institute of Biological and Environmental Sciences, University of Aberdeen, King's College, Aberdeen AB24 3FX, UK.

E-mail: Muhammad.Naveed@abdn.ac.uk; Ph: +441224272258

Abstract

Prediction and modeling of localized flow processes in macropores is of crucial importance for sustaining both soil and water quality. However, currently there are no reliable means to predict preferential flow due to its inherently large spatial variability. The aim of this study was to investigate the predictive performance of previously developed empirical models for both water and air flow and to explore the potential applicability of X-ray Computed Tomography (CT) derived macropore network characteristics. For this purpose, 65 cylindrical soil columns (6 cm diameter and 3.5 cm height) were extracted from the topsoil (5 cm to 8.5 cm depth) in a 15 m × 15 m grid from an agricultural field located in Silstrup, Denmark. All soil columns were scanned with an industrial X-Ray CT scanner (129 µm resolution) and later employed for measurements of saturated permeability, air permeability at -30 cm and -100 cm matric potentials, and gas diffusivity at -30 cm and -100 cm matric potentials. Distribution maps for both permeabilities and gas diffusivities reflected no autocorrelation irrespective of the soil texture and organic matter contents. Existing empirical predictive models for permeabilities showed poor performance, as they were not able to realistically capture macropore flow. The tested empirical model for gas diffusivity predicted measurements at -100 cm matric potential reasonably well, but failed at -30 cm matric potential, particularly for soil columns with biopore-dominated flow. X-ray CT derived macroporosity matched the measured air-filled porosity at -30 cm matric potential well. Many of the CT derived macropore network characteristics were strongly interrelated. Most of the macropore network characteristics were also significantly correlated with saturated permeability, air permeability, and gas diffusivity. The predictive Ahuja et al. (1984) model for saturated permeability, air permeability, and gas diffusivity performed reasonably well when parameterized with novel, X-ray CT derived parameters such as effective percolating macroporosity for biopore-dominated flow and total macroporosity for matrix-dominated

flow. The obtained results further indicate that it is crucially important to discern between matrix-dominated and biopore-dominated flow for accurate prediction of macropore flow from macropore network characteristics.

1. Introduction

The importance of macropore flow for the partitioning of precipitation between runoff and infiltration, for plant water uptake and plant growth, for biogeochemical cycling rates, and for potential risks of ground water contamination is widely recognized (Iversen et al., 2011; de Jonge et al., 2004; Fox et al., 2004; Moustafa, 2000). Thus, over the last decade, major research efforts have been devoted to improve the understanding of macropore flow and associated governing parameters, and to develop predictive macropore flow models (Jarvis, 2007). Macropore flow and transport refers to the localized and commonly very rapid movement of water and solutes through the soil profile. Macropores resulting from biological activity (root channels, worm holes etc.), geological forces (subsurface erosion, shrinkage and swelling etc.), and agricultural management (e.g., plowing) serve as the main channels for this rapid and long-distance flow and transport of water, air, and contaminants. Macropore flow is largely determined by soil structure and is generally a dominating process in loamy and clayey soils (Jarvis et al., 2009) where large inter-aggregate pores and biopores often act as pathways for rapid flow and transport. The transition from matrix to macropore flow (equilibrium to non-equilibrium) depends on the pore size distribution and pore continuity, and the degree of soil saturation (Bouma, 1981). Macropore flow often occurs in pores with equivalent effective cylindrical diameters larger than 0.3 mm, which indicates that the matric potential needs to be close to zero and the water content close to saturation for these pores to be activated (Jarvis, 2007).

Soil and crop management practices strongly modify soil structure and thus the extent of macropore flow and transport. Wang et al. (2013) and Gonzalez-Sosa et al. (2010) studied the impact of land use on the hydraulic properties of the topsoil of the Loess Plateau of China and for a suburban catchment in France, respectively. Both studies have reported greater saturated hydraulic conductivities for forested land, intermediate for permanent pasture, and lower for farmland soils. This is primarily due to the abundance of biota and less disturbance in forests and permanent pastures when compared to cultivated lands (Naveed et al., 2014a; Norgaard et al., 2013; Pérèsa et al., 2012). Application of animal manure and fertilizers can also influence macropore flow, first by altering soil structure and second by promoting the density of earthworms, particularly deep penetrating anecic worms (Naveed et al., 2014b). Climatic conditions (seasonal temperature and precipitation variations) might also affect soil structure and macropore flow through interactions with physical processes such as cyclic freezing/thawing and wetting/drying (Hu et al., 2012). Due to the complex interactions and the significant number of influencing factors, a large spatial variability of saturated hydraulic conductivity has been reported by several authors (Wang et al., 2013; Raczkowski et al., 2012; Iversen et al., 2011). Therefore, the predictive capabilities of empirical models/pedotransfer functions for saturated hydraulic conductivity are limited because they ignore the effects of key site factors and underestimate the significance of soil structure (Vereecken et al., 2010). Recently, pedotransfer functions for saturated hydraulic conductivity that account for soil structure have been developed, but they are rarely applied due to the complexity of input parameters and the still significant prediction inaccuracies (Jarvis et al., 2013; Iversen et al., 2011; Lilly et al., 2008).

Along with the prediction of macropore water flow (i.e. saturated hydraulic conductivity), prediction of macropore airflow (i.e. air permeability and diffusivity) is also of essence. Air permeability is a key parameter for the design of soil vapor extraction remediation processes. Air diffusivity is of importance because the availability of oxygen to plant roots via diffusion is a basic factor of soil productivity. Various empirical models have been proposed in the past for the prediction of air permeability (Deepagoda et al., 2011; Kawamoto et al., 2006) and air diffusivity (Deepagoda et al., 2011; Moldrup et al., 2000).

However, none of the above studies have evaluated their applicability after discerning between biopore- and matrix-dominated flow domains.

Recent developments in soil imaging techniques not only allow visual observations but also quantification of pore network complexity. Application of X-ray CT provides emerging alternative means for estimating subsurface macropore flow and transport (Wildenschild and Sheppard, 2013). Over the last decade, numerous studies about the characterization of macropore structure (i.e. macroporosity, macropore size distribution, volume, surface area, tortuosity, etc.) were conducted with X-Ray CT for different land use and management systems (Katuwal et al., 2015; Larsbo et al., 2014; Hu et al., 2014; Naveed et al., 2013; Vogel et al., 2010; Luo et al., 2010). However, to date there are only a very few published studies on quantitatively relating macropore network characteristics to the observations of macropore flow. Katuwal et al. (2015) found that CT derived macroporosity for the limiting section of the soil column was strongly correlated with air permeability and 5% tracer arrival time. Larsbo et al. (2014) reported significant correlations between X-ray CT derived macropore network characteristics and flow and transport parameters. Paradelo et al. (2013) found that CT derived macroporosity was strongly correlated with saturated hydraulic conductivity, solute dispersivity, and contaminant breakthrough. Luo et al. (2010) reported that macroporosity, path number, hydraulic radius, and macropore angle were the most useful X-ray CT derived parameters for predicting macropore flow and transport under saturated conditions.

In this study we first evaluate the predictive performance of existing pedotransfer functions/models for saturated permeability, air permeability, and gas diffusivity. While it has been previously demonstrated that water flow in macropores cannot be accurately predicted with empirical models from basic soil properties (Vereecken and Javaux, 2009; Vereecken et al., 2010), there is only little published work related to gas diffusivity. Furthermore, existing pedotransfer functions/empirical models do not discern between matrix- and biopore-dominated flow domains, which is of significance for accurate prediction of preferential flow as demonstrated in the results section. In the second part of this study we derive novel macropore network characteristics for saturated permeability, air permeability, and gas diffusivity from X-ray CT observations and demonstrate their utility for improving accuracy of gas and water flow predictions. The simplest form of the Kozeny-Carman equation proposed by Ahuja et al. (1984) is parameterized with novel CT derived parameters such as percolating macroporosity for biopore-dominated flow and total macroporosity for matrix-dominated flow and improvement of prediction accuracy is discussed.

2. Materials and Methods

2.1 Study site and soil sampling

The 1.69-hectars study site located in Silstrup in northwestern Denmark (56° 55′ 56″ N, 8°38′44″ E) is composed of glacial till, a dominant geological formation covering about 43% of all farmland in Denmark (Geological Survey of Denmark and Greenland, 1999). The top meter of the soil is highly fractured and bioturbated, containing 100 biopores per m^2 to 1000 biopores per m^2. The field has not been tilled for about 3 years prior to soil sampling. It has been plowed in December 2008 to 23-cm depth and harrowed twice to 5-cm depth in March 2009. Since then the soil was only disturbed when slurry was injected in 10-cm depth in April 2009 and in 5-cm depth in September 2009. A thorough overview of management practices at the study site between 2006 and 2010 is provided in Norgaard et al. (2013).

Sixty-five undisturbed cylindrical soil cores (6-cm internal diameter and 3.5-cm height) were extracted from the topsoil (5 cm to 8.5 cm depth) in the summer 2012. At the time of sampling the field was cultivated with red fescue (*Festuca rubra* L.). The soil columns were sampled on a 15 m x 15 m grid with additional 5 sampling locations between grid points (Figure 2). All soil columns were extracted by pushing a customized core sampler with aluminum sampling cylinders into the soil and removing the surrounding material step by step. Extracted soil columns were immediately covered with tight plastic lids, placed in plastic bags, and carefully transported to the laboratory to avoid smearing and compaction effects. The soil columns were stored in an environmentally controlled room at 2 °C until the start of measurements. In addition, bulk soil samples were collected from each point at the same soil depth for texture and organic carbon analysis.

2.2 X-ray Computed Tomography scanning and analysis

An industrial X-Ray CT scanner (X-Tek HMX225) at the Helmholtz Center for Environmental Research in Halle in Germany was used to scan the intact soil columns at a voltage of 180 kV and a current of 400 μA. A copper filter was placed between the X-ray source and the soil columns to alleviate beam hardening. The shadow projections (radiographs) were reconstructed with a Feldkamp cone-beam algorithm (Feldkamp et al., 1984) to obtain 16-bit grayscale 3-D data comprised of (500×500×300) voxels at a resolution of 129 μm (Fig. 1a). For subsequent analysis, the 3-D grayscale volumes were cropped to remove the container wall and disturbed regions on the top and bottom of the sample, numerically corrected for intensity differences caused by beam hardening and other scanning artifacts with a sequential algorithm developed by Iassonov and Tuller (2010), and a 3-D median filter (Jassogne et al., 2007) with a radius of 6 voxels was applied to the grayscale volumes to remove noise (Fig. 1b). Though, median filtering is computationally more demanding than conventional smoothing filters, it is less sensitive to outlier values and thus preserve edges. A locally adaptive Bayesian Markov random field (MRF) algorithm (Iassonov et al., 2009; Kulkarni et al., 2012) that was seeded with adaptive K-means clustering (Chen et al., 1998) was used to segment the intensity-corrected and filtered data to distinguish macropores from the soil matrix (Fig. 1c). The homogeneity parameter β in the MRF model was set to 2.0. For details of the applied MRF segmentation algorithm, see Kulkarni et al. (2012) and Tuller et al. (2013).

The segmented CT-data for each soil column were further analyzed to obtain macroporosity, percolating macroporosity, effective percolating macroporosity, macropore specific surface area, macropore hydraulic radius, macropore mean diameter, macropore fractal dimension, macropore global connectivity, and macropore local connectivity (see flowchart depicted in Fig. 1) with the Image-J software package (Rasband, 2011). Three-dimensional pore visualization was conducted with the Image-J plugin 3D viewer. Based on

3D visual observations, soil columns containing percolating biopores (round shaped either formed by roots or earthworms) were separated and labeled as biopore-dominated flow columns; the remaining were labeled as matrix-dominated flow columns (Fig. 1d). The number of pore voxels was determined from the segmented data, and macroporosity (MP) was then calculated as the ratio of the number of pore voxels to the number of total sample voxels (Fig. 1d). The percolating macroporosity (PMP) was calculated based on only the pores that were connected from core sample top to bottom by removing all isolated pores (Fig. 1e). All isolated pores were removed with the Image-J plugin “Find Connected Regions”. Effective percolating macroporosity (EPMP) was defined and calculated as the ratio of minimum cross-sectional area of percolating macropores (while moving voxel layer by voxel layer from the top to the bottom of the core) to the cross-sectional area of the soil column (Fig. 1f). Macropore specific surface (MPSSA) area was calculated as the ratio of surface area of macropores to the volume of soil column (Fig. 1g). It was calculated with the Image-J plugin “Analyze Particles”. Macropore hydraulic radius (MPHR) was defined as the ratio of macropore volume to the macropore surface area (Fig. 1h). It was also calculated with the Image-J plugin “Analyze Particles”. The macropore mean diameter (MPMD) was estimated with a local 3D thickness algorithm proposed by Dougherty and Kunzelmann (2007) and embedded in the Image-J plugin “Bone-J”. This algorithm defines the pore diameter as the diameter of the largest sphere that fits within the pore. The histogram of the thickness map was used for estimating macropore size distribution and macropore mean diameter (Fig. 1i). Macropore fractal dimension (MPFD) was calculated as a measure of the heterogeneity of the spatial distribution of macroporosity with the Image-J plugin “Bone-J” (Fig. 1j). Macropore global connectivity (MPGC) was defined and calculated as the ratio of percolating macroporosity to the total macroporosity of the soil column (Fig. 1k). The macropore local connectivity (MPLC) was estimated with the Image J plugin "Bone-J" (Fig. 1l)

2.3 *Soil physical measurements*

Soil texture was determined from disturbed soil samples using a combination of wet sieving and the hydrometer method, after passing the sample through a 2-mm sieve. Soil organic carbon was determined with a LECO carbon analyzer (St. Joseph, MI, USA) coupled with an infrared CO_2 detector. A multiplication factor of 1.72 was used to convert soil organic carbon to soil organic matter.

After X-ray CT scanning, air permeability and gas diffusivity at -30 cm and -100 cm matric potentials, and saturated hydraulic conductivity were measured on the same columns. The soil columns were placed in a sand box and saturated from the bottom with tap water. After saturation, suction was successively applied to establish matric potentials of -30 cm and -100 cm. Air permeability (k_a) was then measured with the steady state method described in Iversen et al. (2001) both at -30 cm and -100 cm matric potentials. The pressure of 5 hPa was applied to assure laminar flow during the measurements. The k_a was calculated from Darcy's equation based on the pressure difference across the core:

$$Q = \frac{k_a \Delta p a_s}{\eta_a L_s} \qquad (1)$$

where Q (L^3 T^{-1}) is the volumetric flow rate, k_a (L^2) is air permeability, Δp (M $L^{-1}T^{-2}$) is the pressure difference across the column, η (M L^{-1} T^{-1}) is dynamic viscosity of air, a_s (L^2) is the cross-sectional area and L_s (L) is the length of the column. Gas diffusivities (D_P/D_0) at -30 cm and -100 cm matric potentials were measured with the one-chamber method described in Schjønning et al. (2013).

After D_P/D_0 measurements, the soil columns were resaturated, and the saturated hydraulic conductivity was measured with the constant head method (Klute and Dirksen, 1986). The laboratory measured saturated hydraulic conductivities were then converted to intrinsic permeabilities considering water at 20 °C:

$$k_{sat} = K_{sat} \frac{\eta_w}{\rho_w} \frac{1}{g} \qquad (2)$$

where k_{sat} (L^2) is saturated permeability, K_{sat} ($L\ T^{-1}$) is saturated hydraulic conductivity, η_w ($M\ L^{-1}\ T^{-1}$) is dynamic viscosity of water, ρ_w ($M\ L^{-3}$) is density of water and g ($L\ T^{-2}$) is gravitational acceleration. Intrinsic permeability was used for better comparison with air permeability measurements. All measured flow parameters are provided in supplementary Table S1.

2.4 Modelling

Ahuja et al., (1984) developed a relationship (EPM, effective porosity model) between saturated hydraulic permeability (k_{sat}) and effective porosity (ϕ_e) based on the generalized Kozeny-Carman equation:

$$k_{sat}\ or\ {}^{D_P}/_{D_0} = A\phi_e^{\,B} \qquad (3)$$

where D_P/D_0 is gas diffusivity, and *A* and *B* are empirical constants. Ahuja et al. (1984) defined ϕ_e as the total porosity minus the soil volumetric water content at field capacity, assumed as the water content at a matric potential of -33 kPa. Rawls et al. (1998) reported that several researchers found the slope *A* to vary between 1.59 and 3.98 and the intercept to vary between 440 cm d^{-1} and 34,000 cm d^{-1}. We have modified equation (3) by using X-ray CT derived macroporosity (MP) as ϕ_e for matrix-dominated flow, and X-ray CT derived effective percolating macroporosity (EPMP) as ϕ_e for biopore-dominated flow.

2.5 Statistics

Data collected for soil textural properties and macropore flow parameters were first subjected to classical statistical analysis to obtain descriptive statistics, including minimum, maximum, mean, median, standard deviation, skewness, and coefficient of variation (CV). The degree of spatial variability of soil textural properties and macropore flow parameters was determined with ordinary kriging. The ArcMap 10.1 (Esri, Inc.) software was used to generate contour maps for each measured soil property. Spearman rank order correlation coefficients between macropore network characteristics and macropore flow parameters were calculated with the commercial SigmaPlot 11.0 software package. The correlations were considered significant if p values were below 0.01. Selected correlations were also graphically displayed and analyzed with linear or power regressions. The form of regression relationship was chosen based on the achievable coefficients of determination (R^2). The power function was preferred over simple linear regression if it resulted in larger R^2. The linear and power models were only fitted if they were significant at $p < 0.01$.

3. Results and Discussion

3.1. *Spatial variability of soil texture, organic matter, and macropore flow parameters*

The soil of the study site was classified as sandy loam (USDA-NRCS Web Soil Survey, 2010) with clay contents ranging from 14 % to 19 %, and organic matter content varying from 2.9 % to 3.8 %. Descriptive statistics for all soil textural properties are depicted in Table 1. Clay and sand contents were positively skewed, whereas silt and organic matter contents were negatively skewed. All soil textural properties were slightly variable across the field with coefficients of variation (CV) below 10 %. It has been previously reported that the CV for soil textural properties generally depends on the extent of the study area. For example, Sharma et al. (2011) reported a CV for soil textural properties within the range of 20 % to 30 % for a 40 ha agricultural field in New Mexico, while Wang et al. (2013) reported a CV within the range of 19 % to 156 % across the Loess Plateau of China (620 × 10^3 km^2). Krigged maps indicated that soils with high clay contents (Fig. 2a) were on the north side of the field, whereas soils with high organic matter contents occupied the south side (Fig. 2d). Thus, clay and organic matter gradients run in opposite directions at the study site. Soils with high silt contents (Fig. 2b) were on the western side of the field, whereas soils with high sand contents were on the eastern side (Fig. 2c).

Descriptive statistics for saturated permeability (k_{sat}), air permeability (k_a), and gas diffusivity (D_P/D_0) at -30 cm and -100 cm matric potentials are provided in Table 1. Large positive skewness and quite different mean and median values were observed for all five macropore flow parameters. The k_{sat}, k_a, and D_P/D_0 at -30 cm and -100 cm matric potentials showed the largest variations across the study site with a CV ranging from 92 % to 218 % (up to 5 orders of magnitude). High CV values were observed due to the presence of biopores in some of the soil columns, while not in others (samples marked as *I*, *II*, *III*, and *IV* in Fig. 2 are shown in Fig. 3; out of the 4 marked samples *I* and *II* are matrix-flow dominated and *III* and *IV* are biopore-flow dominated). Irrespective of the extent of the study area, large variations in k_{sat} were also reported in other studies (e.g., Wang et al., 2013; Sharma et al., 2011; and Iqbal et al., 2005). Krigged maps for k_{sat}, k_a, and D_P/D_0 (Figs. 2e-g) look quite similar with some areas randomly exhibiting a high level of macropore flow while matrix flow dominated in other regions irrespective of soil texture and organic matter content.

3.2. Predictive performance of empirical models

For many hydrological applications, saturated permeability (k_{sat}) is estimated from more readily available proxy variables such as texture and bulk density. Various empirical models/pedotransfer functions (e.g. Iversen et al., 2011; Jarvis et al., 2009; Schaap et al., 2001; Wösten et al., 1999; Revil and Cathles, 1999) have been previously proposed for predicting saturated hydraulic conductivity. We have observed poor predictive performance of empirical k_{sat} models such as proposed by Revil and Cathles (1999) and Schaap et al. (2001) (Fig. 4) and for models proposed by Wösten et al. (1999), Vereecken et al. (1989), and Cosby et al. (1984) (not shown). While the measured saturated permeabilities spanned five orders of magnitude, model predictions were within a narrow range (Fig. 4). This reflected the presence of a wide range of macropores and biopores in the soil columns. The primary reason for the failure of the existing empirical models/pedotransfer functions is that they are based on soil texture and bulk density, and thus are not able to realistically capture macropore flow, particularly for highly structured and bioturbated soils. In general, empirical models over-predicted k_{sat} in case of matrix flow (empty symbols), while they under-predicted k_{sat} for soil columns with biopore flow (filled symbols). Because results were obtained for samples of limited size from the A-horizon, it should be noted that for larger scales the structural characteristics, especially that related to pore connectivity, might change and herewith also the flow parameters.

Over the last 2 decades, some efforts were also devoted to the development of empirical models for the prediction of air permeability (k_a) (Moldrup et al., 1998; Kawamoto et al., 2006; Deepagoda et al., 2011). Here, we have tested the predictive performance of the recently developed density-corrected k_a model (Deepagoda et al., 2011) as shown in Figures 5a and 5b. The density-corrected k_a model performed reasonably well for soils with lower k_a values (some of the columns with matrix-dominated flow), but completely failed for soils with greater k_a values for example in the presence of continuous structural cracks or biopores. Starting with Buckingham (1904) a more rigorous effort has been made in the previous century to develop empirical models for the prediction of gas diffusivity (Deepagoda et al., 2011). The tested WLR-Marshall model (Moldrup et al., 2000) predicted gas diffusivity reasonably well for soil samples associated with matrix flow and underestimated gas diffusivity for soil samples with biopore flow at -30 cm matric potential (Fig. 5c). This reflects that preferential diffusive flow could occur at greater matric potentials close to saturation even though gas diffusivity is a concentration-driven gas transport parameter. However at -100 cm matric potential, the WLR-Marshall model (Moldrup et al., 2000) predicted gas diffusivity well for all soil samples irrespective of matrix or biopore flow (Fig. 5d).

3.3. Correlations between macropore flow parameters and macropore network characteristics

The CT-derived macroporosity was plotted as a function of physically measured air-filled porosity at -30 cm matric potential (Fig. 6). The physically measured air-filled porosity at -30 cm matric potential agreed well with the X-ray CT analyzed macroporosity at 129-µm resolution. At -30 cm matric potential, all pores of diameter larger than 100 µm should have drained according to the Young Laplace capillary-rise equation. Referring to this, physically measured air-filled porosity at -30 cm matric potential (pore diameter > 100 μm) should be greater than the X-ray CT derived macroporosity (resolution = 129 μm). However, this is only true when assuming a parallel bundle of capillary tubes, which is clearly not realistic for natural soils. Due to the ink-bottle effect a considerable volume of pores of diameter > 100 μm are expected to be water filled after drainage at a water potential of -30 cm. Hence, no perfect match between the morphological pore size measured with CT and the hydraulic pore size estimated from the Young-Laplace equation can be expected (Vogel, 2000). Hence, the observed agreement between the two measures is absolutely reasonable and confirms the accuracy of the employed image segmentation method (Fig. 6). However, it must be noted that different image segmentation methods can result in quite different macroporosity values if the image quality is bad, i.e. there is a lot of noise and partial volume effect as shown in Naveed et al. (2014c).

Spearman rank order correlation analysis between macropore flow parameters and macropore network characteristics was carried out first for all soil columns (Fig. 7a), second for soil columns containing biopores(s) connected from top to bottom (Fig. 7b), and third for soil columns containing inter-aggregate macropores or disconnected biopores (Fig. 7c). Many of the CT-derived macropore network characteristics were strongly inter-related (Fig. 7). This is because large macroporosities were associated with larger macropore surface area and better connectivity of macropores. This is in agreement with other recent studies (e.g., Katuwal et al., 2015; and Larsbo et al., 2014). Macropore mean diameter and hydraulic radius were however poorly correlated with other macropore network characteristics because of inherently different measures of macropores. Significant spearman rank order correlations were also observed between macropore flow parameters and most of the CT-derived macropore network characteristics (Fig. 7). X-ray CT macroporosity was strongly correlated with macropore flow parameters for all three categories of soil samples (Figs. 7a, b, and c).

Very strong correlations were observed between effective percolating macroporosity (EPMP) and macropore flow parameters for the soil columns consisting of biopores(s) connected from top to bottom (Fig. 7b). Macropore hydraulic radius and macropore mean diameter were significantly correlated with macropore flow parameters for the soil columns associated with biopore-dominated flow (Fig. 7b), whereas poorly correlated in case of soil columns associated with matrix-dominated flow (Fig. 7c). Elliot et al. (2010) and Quinton et al. (2008) support this. Both macropore global and local connectivities were poorly correlated with macropore flow parameters for the soil columns associated with biopore-dominated flow (Fig. 7b), whereas significantly correlated for the soil columns associated with matrix-dominated flow (Fig. 7c). This makes sense as biopore flow is mainly controlled by the size of the largest biopore present in the soil columns, whereas matrix flow is mainly controlled by the pore size distribution and connectivity of pores.

Selected correlations were graphically displayed and analyzed with linear and power regressions (which best described the data) as shown in Figure 8. The saturated permeability (k_{sat}) was plotted as a function of CT-derived macroporosity (8a). A two-branch data trend was observed at lower CT derived macroporosity, which merges into a single branch with the increase of macroporosity. The upper branch with greater permeabilities consists of soil columns with one or more biopores connected from top to bottom that mainly governs fluid flow (filled symbols). Samples *III* and *IV* marked in Figure 8a and shown in Figure 3 are members of this branch. The lower branch consists of soil samples in which fluid mainly flows through inter-aggregate and textural pores (unfilled symbols). Samples *I* and *II* marked in Figure 8a and shown in Figure 3 are members of this branch. Significant distinct power regressions were observed between k_{sat} and macroporosity for these two categories of the soil columns (Fig. 8a). This suggests that distinction between biopore-dominated flow and matrix-dominated flow should be carried out as a first step in studying the relationships between macropore flow and CT-derived macroporosity. Both Paradelo et al. (2013) and Luo et al. (2010) found similar relationships between saturated hydraulic conductivity and CT derived macroporosity with R^2 ranging from 0.50 to 0.60. A stronger power regression was observed, R^2 increased from 0.43 to 0.76, when k_{sat} was plotted as a function of the effective percolating macroporosity for the soil columns associated with biopore-dominated flow (Fig. 8b, filled symbols), but this is not the case for the soil columns with matrix-dominated flow (Fig. 8b, empty symbols). Significant power regressions were observed between k_{sat} and macropore mean diameter (Fig. 8c). Weak, but significant power regression was observed between k_{sat} and macropore local connectivity for only those soil columns associated with matrix-dominated flow as shown in Figure 8d. No significant regression was observed between k_{sat} and macropore local connectivity for the soil samples associated with biopore-dominated flow (Fig. 8d, filled symbols). A potential explanation is that the Euler number that is the basis for macropore local connectivity calculations does not account for continuity of the pores from top to bottom.

Air permeability at -30 cm matric potential, k_a (-30), was plotted as a function of macroporosity as shown in Figure 8e. Significant distinct power regressions were observed for the two categories of soil columns i.e. biopore-dominated flow and matrix-dominated flow (Fig. 8e). Similarly to k_{sat}, power regression was significantly improved (R^2 increased from 0.49 to 0.80) when k_a (-30) was plotted as a function of effective percolating macroporosity instead of total macroporosity for the soil columns associated with biopore-dominated flow (Fig. 8f, filled symbols). A significant power regression was observed between k_a (-30) and macropore mean diameter for the soil columns with biopore-dominated flow while no significant regression was observed between k_a (-30) and macropore mean diameter for the soil columns with matrix-dominated flow (Fig. 8g). Contrary to this, significant power regression was observed between k_a (-30) and macropore local connectivity for soil columns associated with matrix-dominated flow while no significant regression was observed for soil samples associated with biopore-dominated flow (Fig. 8h). Similar power regressions were also observed for k_a (-100) as a function of macroporosity, effective percolating macroporosity, macropore mean diameter, and macropore local connectivity as shown in Figures 8i, 8j, 8k, and 8l, respectively.

Figures 8m and 8n showed significant power regressions when gas diffusivity at -30 cm matric potential, D_P/D_0 (-30), was plotted against macroporosity and effective percolating macroporosity, respectively. Distinct significant power regressions observed for soil columns associated with biopore-dominated flow and matrix-dominated flow reflects that preferential diffusive flow occurred at -30 cm matric potential. However at -100 cm matric potential, a single regression significantly described both types of data associated with biopore flow and matrix flow as shown in Figures 8q and 8r. This reflects that no preferential diffusive flow occurred at and below -100 cm matric potentials. Both D_P/D_0 (-30) and D_P/D_0 (-100) showed insignificant regressions when plotted as a function of macropore mean diameter for both categories of soil samples (Figs. 8o and 8s). Significant power regressions were observed when D_P/D_0 (-30) and D_P/D_0 (-100) were plotted as a function of macropore local connectivity for both set of soil columns associated with matrix flow and biopore flow (Figs 8p and 8t). This is logical as D_P/D_0 is a concentration-driven gas transport parameter and is mainly controlled by total air-filled pore space and its connectivity, and not by the pore size (Moldrup et al., 2000).

3.4. Modelling saturated permeability, air permeability and diffusivity

Saturated permeability, air permeability at -30 cm and -100 cm matric potentials, and gas diffusivity at -30 cm and -100 cm matric potentials were modelled using the simplified form of Kozeny-Carman equation presented by Ahuja et al. (1984). We have modified this equation by providing novel input parameters. The effective porosity in the original model was replaced with the CT derived total macroporosity (MP) in case of matrix-dominated flow, and with the effective percolating macroporosity (EPMP) in case of biopore-dominated flow. The empirical fitting parameters (A and B) for saturated permeability, air permeability at -30 cm and -100 cm matric potentials, and gas diffusivity at -30 cm and -100 cm matric potentials are given in Table 3. The 1:1 plots between measured and predicted saturated permeability, air permeability, and gas diffusivity are shown in Figure 9. From figure 9 it is obvious that predictions with the simplified Kozeny-Carman equation with novel input data from X-ray CT analysis are very reasonable. However, the predictive capability of the proposed modelling framework requires further independent validation for different soil types to confirm the values/ranges for empirical constants A and B for saturated permeability, air permeability, and gas diffusivity.

Rapid development of advanced CT-image segmentation and analysis tools in conjunction with computational fluid dynamics provide promising future means to simulate the dynamics of flow and transport directly with CT derived macropore networks as boundaries. One method particularly suitable for simulating macropore flow and transport based on X-ray CT data is the lattice Boltzmann method (LBM). Most of the studies to date that applied the LBM for simulating flow and transport based on CT-data were for granular porous media (glass beads/sand) and fractured rocks, and not for natural field soil samples. Strong correlations between macropore flow parameters and X-ray CT derived macropore network characteristics suggest that lattice Boltzmann flow and transport simulations based on X-ray CT images could be a potential topic for future research and pave the way for the establishment of a digital soil physics laboratory.

4. Conclusions and Perspective

1. Soil textural properties showed small spatial variability across the study site with a CV $<$ 10%. Despite this, macropore flow parameters i.e. saturated permeability, air permeability, and gas diffusivity, showed large spatial variability across the field with a CV $>$ 100%.
2. Predictive performance of existing empirical models/pedotransfer functions for saturated permeability and air permeability at -30 cm and -100 cm matric potentials was quite poor. For saturated permeability, existing empirical models over predicted in case of matrix-dominated flow and under predicted in case of biopore-dominated flow. For air permeabilities, empirical models predicted matrix-dominated flow reasonably, whereas under predictions were observed in cases of biopore-dominated flow. The tested empirical model for the prediction of gas diffusivity performed well at -100 cm matric potential, while it failed at -30 cm matric potential particularly for the soil columns that contained top-to-bottom connected biopores i.e. biopore dominated flow.
3. Significant Spearman's Rank correlations were observed between CT-derived macropore network characteristics and macropore flow parameters. These correlations were further improved by splitting soil columns into matrix-dominated flow columns and biopore-dominated flow columns. The predictive performance of Ahuja et al. (1984) model with novel input parameters, X-ray CT derived effective percolating macroporosity (EPMP) for biopore-dominated flow and total macroporosity (MP) for matrix-dominated flow, was very good. However, further studies for different soil types are needed to confirm the values/ranges of empirical constants A and B of Ahuja et al., (1984) model for robust predictions of saturated permeability, air permeability, and gas diffusivity.

Authors Contributions

Muhammad Naveed, Per Moldrup, Lis Wollesen de Jonge, and Markus Tuller designed the study and wrote the manuscript. Marcel Schaap and Hans-Jörg Vogel assisted with X-ray CT scanning and analysis. Ramaparsad Kulkarni performed image segmentation. All authors contributed to the manuscript with comments and suggestions throughout the writing process.

Acknowledgements

The technical assistance of Stig T. Rasmussen, Bodil B. Christensen, and Michael Koppelgaard are greatfully acknowledged. The study was part of the Soil Infrastructure, Interfaces, and Translocation Processes in Inner Space (Soil-it-is) project, which is funded by the Danish Research Council for Technology and Production Sciences.

References

Bouma, J. (1981), Comments on micro- meso- and macroporosity of soil, SSSAJ, 45, 1244-1245.

Buckingham, E. 1904. Contributions to our knowledge of the aerations of soils. Bur. Soil Bull. 25. U.S. Gov. Print. Office, Washington, DC.

Chen, C.W., J. Luo, and K.J. Parker (1998), Image segmentation via adaptive K-mean clustering and knowledge-based morphological operations with biomedical applications. IEEE Trans. Image Process. 7:1673–1683. doi:10.1109/83.730379

Cosby, B. J., G. M. Hornberger, R. B. Clapp, and T. R. Ginn (1984), A statistical exploration of the relationships of soil moisture characteristics to the physical properties of soils, Water Resources Research, 20, 682-690.

Deepagoda, C., P. Moldrup, L. W. de Jonge, K. Kawamoto, T. Komatsu (2011), Density-corrected models for gas diffusivity and air permeability in unsaturated soil, Vadose Zone Journal, 10, 226-238.

de Jonge, L.W., P. Moldrup, G. H. Rubaek, K. Schelde, and J. Djurhuus (2004), Particle leaching and particle-facilitated transport of phosphorus at field scale, Vadose Zone Journal, 3, 462–470.

Dougherty, R., and K. Kunzelmann. 2007. Computing local thickness of 3D structures with Image J. Microscopy Microanalysis, 13: 1678-1679. doi: 10.1017/S1431927607074430.

Elliot, T. R., W. D. Reynolds, and R. J. Heck (2010), Use of existing pore models and X-ray computed tomography to predict saturated soil hydraulic conductivity, Geoderma, 156, 133-142.

Feldkamp, L. A., L. C. Davis, and J. W. Kress (1984), Practical cone-beam algorithm, J. Opt. Soc. Am. A1, 612–619.

Fox, G. A., R. Malone, G. J. Sabbagh, and K. Rojas (2004), Interrelationship of macropores and subsurface drainage for conservative tracer and pesticide transport, J. Environ. Qual. 33, 2281-2289, doi:10.2134/jeq2004.2281.

Geological Survey of Denmark and Greenland. 1999. Digitalt kort over Danmarks jordarter 1:200000; GEUS rapport 1999/47. (In Danish.) Geological Survey of Denmark and Greenland, Copenhagen, Denmark.

Gonzalez-Sosa, E., I. Braud, J. Dehotin, L. Lassabatere, R. Angulo-Jaramillo, M. Lagouy, F. Branger, C. Jacqueminet, S. Kermadi and K. Michel (2010), Impact of land use on the hydraulic properties of the topsoil in a small French catchment, Hydrol. Processes, 24, 2382-2399.

Hu, Y., J. Feng, T. Yang, and C. Wang (2014), A new method to characterize the spatial structure of soil macropore networks in effects of cultivation using computed tomography, Hydrological Processes, 28, 3419-3431.

Hu, W., M. A. Shao, and B. C. Si (2012), Seasonal changes in surface bulk density and saturated hydraulic conductivity of natural landscapes, Eur. J. of Soil Science, 63, 820-830.

Iassonov, P., T. Gebrenegus, and M. Tuller (2009), Segmentation of X-ray computed tomography images of porous materials: A crucial step for characterization and quantitative analysis of pore structures. Water Resour. Res. 45(9):W09415. doi:10.1029/2009wr008087

Iassonov, P., and M. Tuller (2010), Application of segmentation for correction of intensity bias in X-ray computed tomography images. Vadose Zone J. 9:187–191. doi:10.2136/vzj2009.0042

Iqbal, J., J. A. Thomasson, J. N. Jenkins, P. R. Owens, and F. D. Whisler (2005). Spatial variability analysis of soil physical properties of alluvial soils, doi:10.2136/sssaj2004.0154.

Iversen, B. V., C. D. Børgesen, M. Lægdsmand, M. H. Greve, G. Heckrath, C. Kjærgaard (2011), Risk predicting of macropore flow using pedotransfer functions, textural maps, and modeling. Vadose Zone Journal, 10, 1185-1195.

Iversen, B. V., P. Schjønning, T. G. Poulsen, and P. Moldrup (2001a), In situ, on-site and laboratory measurements of soil air permeability: Boundary conditions and measurement scale, Soil Sci., 166, 97-106.

Jarvis, N., J. Koestel, I. Messing, J. Moeys, and A. Lindahl (2013), Influence of soil, land use and climate factors on the hydraulic conductivity of soil, Hydrol. Earth Syst. Sci., 17, 5185-5195.

Jarvis, N. J., J. Moeys, J. M. Hollis, S. Reichenberger, A. M. L. Lindahl, and I.G. Dubus (2009), A conceptual model of soil susceptibility to macropore flow, Vadose Zone J. 8, 902–910, doi:10.2136/vzj2008.0137.

Jarvis, N.J. (2007). A review of non-equilibrium water flow and solute transport in soil macropores: Principles, controlling factors and consequences for water quality, Eur. J. Soil Sci., 58, 523–546, doi:10.1111/j.1365-2389.2007.00915.

Jassogne, L., A. McNeill, and D. Chittleborough (2007), 3D visualization and analysis of macro- and meso-porosity of the upper horizons of sodic, texture-contrast soil, Eur. J. Soil Sci., 58, 589–598, doi:10.1111/j.1365-2389.2006.00849.

Katuwal, S., T. Nørgaard, P. Moldrup, M. Lamandé, D. Wildenschild, and L. W. de Jonge (2015). Linking air and water transport in intact soils to macropore characteristics inferred from X-ray computed tomography, Geoderma, 237–238, 9–20, doi:10.1016/j.geoderma.2014.08.006.

Kawamoto, K., P. Moldrup, P. Schjønning, B. V. Iversen, T. Komatsu, and D. E. Rolston (2006) Gas transport parameters in the vadose zone: Development and test of power-law models for air permeability, Vadose Zone J., 5, 1205-1215.

Klute, A., and C. Dirksen (1986), Hydraulic conductivity and diffusivity: Laboratory methods. In Methods of Soil Analysis, Part 1, 2nd Ed. Physical and Mineralogical Methods. A Klute (ed.). ASA-SSSA, Madison, WI, 687-734.

Kulkarni, R., M. Tuller, W. Fink, and D. Wildenschild (2012), Three-dimensional multiphase segmentation of X-ray CT data of porous materials using a Bayesian Markov random field framework, doi:10.2136/vzj2011.0082.

Larsbo, M., J. Koestel, and N. Jarvis (2014) Relations between macropore network characteristics and the degree of preferential solute transport, Hydrol. Earth Syst. Sci., 18, 5255–5269, 2014.

Lilly, A., A. Nemes, W. J. Rawls, and Y. A. Pachepsky (2008), Probabilistic approach to the identification of input variables to estimate hydraulic conductivity, Soil Sci. Soc. Am. J., 72, 16-24.

Luo, L., H. Lin, and J. Schmidt (2010), Quantitative relationships between soil macropore characteristics and preferential flow and transport, Soil Sci. Soc. Am. J., 74, 1929–1937.

Moldrup, P., T. Olesen, J. Gamst, P. Schjønning, T. Yamaguchi, and D.E. Rolston. 2000. Predicting the gas diffusion coefficient in repacked soil: Water induced linear reduction model. Soil Sci. Soc. Am. J. 64:1588–1594.

Moldrup, P., T. G. Poulsen, P. Schjønning, T. Olsen, and T. Yamaguchi (1998), Gas permeability in undisturbed soils: Measurements and predictive models, Soil Sci., 163, 180-189.

Moustafa, M. M. (2000), A geostatistical approach to optimize the determination of saturated hydraulic conductivity for large-scale subsurface drainage design in Egypt, doi: 10.1016/S0378-3774(99)00042-6.

Naveed, M., P. Moldrup, E. Arthur, M. Holmstrup, M. Nicolaisen, M. Tuller, L. Herath, S. Hamamoto, K. Kawamoto, T. Komatsu, H-J Vogel, and L. W. de Jonge (2014a), Simultaneous Loss of Soil Biodiversity and Functions Along a Copper Contamination Gradient: When Soil Goes to Sleep, doi: 10.2136/sssaj2014.02.0052.

Naveed, M., P. Moldrup, H-J. Vogel, M. Lamandé, D. Wildenschild, M. Tuller, and L. W. de Jonge (2014b). Impact of long-term fertilization practice on soil structure evolution, Geoderma, 217-218, 181-189.

Naveed, M. (2014c). Revealing soil architecture and quality: Linking state-of-the-art soil biophysicochemical measurements, visualizations, and simulations. PhD thesis, Aarhus University.

Naveed, M., P. Moldrup, E. Arthur, D. Wildenschild, M. Eden, M. Lamande, H-J. Vogel, and L. W. de Jonge (2013), Revealing soil structure and functional macroporosity along a clay gradient using X-ray computed tomography, Soil Sci. Soc. Am. J., 77, 403–411.

Norgaard, T., P. Moldrup, P. Olesen, A. L. Vendelboe, B. V. Iversen, M. H. Greve, J. Kjaer, and L. W. de Jonge (2013), Comparative mapping of soil physical-chemical and structural parameters at field scale to identify zones of enhanced leaching risk, J. Environ. Qual. 42, 271-283.

Otsu, N. 1975. A threshold selection method from gray-level histograms. Automatica, 11(285-296): 23-27.

Paradelo, M., P. Moldrup, E. Arthur, M. Naveed, M. Holmstrup, J. E. López-Periago, L. W. de Jonge (2013), Effects of Past Copper Contamination and Soil Structure on Copper Leaching from Soil, doi: 10.2134/jeq2013.05.0209.

Pérèsa, G., A. Bellidoa, P. Curmib, P. Marmonierc, and D. Cluzeaua (2012), Relationships between earthworm communities and burrow numbers under different land use systems, Pedobiologia, 54, 37–44.

Quinton, W. L., M. Hayashi, and S. K. Carey (2008), Peat hydraulic conductivity in cold regions and its relation to pore size and geometry, Hydrol. Proc., 22, 2829-2837.

Rasband, W.S. (2011) Image-J. U.S. National Institutes of Health, Bethesda, Maryland, USA (http://imagej.nih.gov/ij/, 1997–2012).

Raczkowski, C. W., J. P. Mueller, W. J. Busscher, M. C. Bell, and M. L. McGraw (2012), Soil physical properties of agricultural systems in a large-scale study, Soil & Tillage Research, 119, 50–59.

Revil, A., and L. M. Cathles (1999), Permeability of shaly sands.Water Resour. Res. 35, 651-662.

Ridler, T., and S. Calvard. 1978. Picture thresholding using an iterative selection method. IEEE Trans. Syst. Man Cybern., 8(8):630-632, doi:10.1109/TSMC.1978.4310039.

Sauvola, J., and M. Pietikainen. 2000. Adaptive document image binarization. Pattern Recognition. 33: 225-236. doi: 10.1016/S0031-3203(99)00055-2.

Schaap, M. G., F. L. Leij, M. T. van Genuchten (2001), Rosetta: A computer programme for estimating soil hydraulic parameters with hierarchical pedotransfer functions, Journal of Hydro., 251, 163-176.

Schjønning, P., M. Eden, P. Moldrup, and L.W. de Jonge. 2013. Two-chamber, two-gas and onechamber, one-gas methods for measuring the soil-gas diffusion coefficient:

Validation and inter-calibration. Soil Sci. Soc. Am. J. 77:729–744. doi:10.2136/sssaj2012.0379.

Sharma, P., M. K. Shukla, and J. G. Mexal (2011), Spatial variability of soil properties in agricultural fields of Southern New Mexico, Soil Sci., 176, 288-302.

Tuller, M., R. Kulkarni, and W. Fink (2013), Segmentation of X-ray CT data of porous materials: A review of global and locally adaptive algorithms. In: S.H. Anderson and J.W. Hopmans, editors, Soil–water–root processes: Advances in tomography and imaging. SSSA Spec. Publ. 61. SSSA, Madison, WI. p. 157–182. doi:10.2136/sssaspecpub61.c8

USDA-NRCS Web Soil Survey (2010), Available from: websoilsurvey.nrcs.usda.gov/app/WebSoilSurvey.aspx.

Vereecken, H., M. Weynants, M. Javaux, Y. Pachepsky, M. G. Schaap, and M. T. van Genuchten (2010), Using pedotransfer functions to estimate the van Genuchten-Mualem soil hydraulic properties: a review, Vadose Zone J., 9, 795-820.

Vereecken, H., J. Maes, J. Feyen, and P. Darius (1989), Estimating the soil moisture retention characteristic from texture, bulk density, and carbon content, Soil Sci, 148, 389-403.

Vogel, H.-J., U. Weller, and S. Schluter (2010), Quantification of soil structure based on Minkowski functions, Comput. Geosci., doi:10.1016/j.cageo.2010.03.007.

Vogel, H.-J., 2000: A numerical experiment on pore size, pore connectivity, water retention, permeability, and solute transport using network models. Europ. J. Soil Sci., 51, 99-105.

Wang, Y., M. Shao, Z. Liu, R. Horton (2013), Regional-scale variation and distribution patterns of soil saturated hydraulic conductivities in surface and subsurface layers in the loessial soils of china, Journal of Hydrology, 487, 13-23.

Weynants, M., H. Vereecken and M. Javaux. (2009), Revisiting Vereecken pedotransfer functions: Introducing a closed-form hydraulic model. Vadose Zone J. 8: 86-95.

Wosten, J. H. M., A. Lilly, A. Nemes, and C. L. Bas (1999), Development and use of a database of hydraulic properties of European soils, Geoderma 90, 169-185.

Wildenschild, D., and A. Sheppard (2013) X-ray imaging and analysis techniques for quantifying pore-scale structure and processes in subsurface porous medium systems, Advances in Water Res., 51, 217-246.

Table 1: Descriptive statistics for selected soil physical properties (n = 65)

Variable	Minimum	Maximum	Mean	Median	Standard deviation	Skewness	CV %
Clay (g $100g^{-1}$)	14.18	18.93	15.82	15.54	1.36	0.65	9
Silt (g $100g^{-1}$)	23.30	33.32	30.12	30.10	1.66	-1.21	6
Sand (g $100g^{-1}$)	44.89	59.00	50.71	50.72	2.14	0.32	4
Organic matter (g $100g^{-1}$)	2.90	3.75	3.35	3.38	0.20	-0.42	6
Saturated hydraulic. conductivity (cm hr^{-1})	0.02	418.2	40.15	1.38	89.48	2.84	218
Saturated permeability, k_{sat} (μm^2)	0.01	118.1	12.04	0.39	26.30	2.73	218
Air permeability at -30 cm, k_a -30, (μm^2)	0.03	109.19	10.87	3.21	22.33	3.03	205
Air permeability at -100 cm, k_a -100, (μm^2)	0.19	151.10	14.72	5.42	27.13	3.26	184
Gas diffusivity at -30 cm, D_P/D_0-30	1.0×10^{-4}	1.8×10^{-2}	2.6×10^{-3}	1.7×10^{-3}	3.0×10^{-3}	2.74	123
Gas diffusivity at -100 cm, D_P/D_0-100	4.0×10^{-4}	2.5×10^{-2}	5.2×10^{-3}	4.0×10^{-3}	5.0×10^{-3}	2.31	92

Table 2: Partial sill, nugget, range, kriging interpolation model, and root mean square error (RMSE) for semivariograms for each interpolated map. All interpolations were carried out in ESRI ArcMap 10.1.

Variable	Partial Sill	Nugget	Range (m)	Model	RMSE
Clay (g $100g^{-1}$)	3.1×10^{-4}	3.6×10^{-5}	179	Gaussian	7.0×10^{-3}
Silt (g $100g^{-1}$)	1.6×10^{-4}	2.2×10^{-4}	200	Gaussian	1.5×10^{-2}
Sand (g $100g^{-1}$)	2.9×10^{-4}	1.8×10^{-4}	61	Spherical	1.7×10^{-2}
Organic matter (g $100g^{-1}$)	3.8×10^{-6}	6.8×10^{-7}	89	Spherical	1.2×10^{-3}
Saturated permeability, k_{sat} (μm^2)	214	538	24	Spherical	27.67
Air permeability at -30 cm, k_a -30, (μm^2)	80	459	24	Circular	23.45
Air permeability at -100 cm, k_a -100, (μm^2)	0	753	0	Spherical	27.54
Gas diffusivity at -30 cm, D_P/D_0-30	2.7×10^{-6}	1.0×10^{-5}	24	Spherical	3.5×10^{-3}
Gas diffusivity at -100 cm, D_P/D_0-100	6.3×10^{-6}	2.1×10^{-5}	30	Circular	5.3×10^{-3}

Table 3: Fitted empirical constants for the Ahuja (1984) model with X-ray CT derived effective percolating macroporosity (EPMP) and total macroporosity (MP) as input parameters for biopore- and matrix-dominated flow, respectively.

Variable	A	B
Biopore-dominated flow		
Saturated permeability, k_{sat} (µm^2)	5000	1.4
Air permeability at -30 cm, k_a -30, (µm^2)	5000	1.5
Air permeability at -100 cm, k_a -100, (µm^2)	5000	1.4
Gas diffusivity at -30 cm, D_P/D_0-30	0.27	1.12
Gas diffusivity at -100 cm, D_P/D_0-100	0.27	0.98
Matrix-dominated flow		
Saturated permeability, k_{sat} (µm^2)	5000	3.6
Air permeability at -30 cm, k_a -30, (µm^2)	5000	3.0
Air permeability at -100 cm, k_a -100, (µm^2)	5000	2.7
Gas diffusivity at -30 cm, D_P/D_0-30	0.27	1.90
Gas diffusivity at -100 cm, D_P/D_0-100	0.27	1.55

Figures Captions:

Figure 1: Flowchart illustrating all performed CT-data enhancement, segmentation, and analysis steps.

Figure 2: Contour maps depicting the spatial distribution of soil textural properties and macropore flow parameters, (a) clay (< 2 µm), (b) silt (2 µm -50 µm), (c) sand (50 µm -2000 µm), (d) organic matter content, (e) saturated permeability (μm^2), (f) air permeability (μm^2) at -100 cm matric potential, and (g) gas diffusivity at -100 cm matric potential. Visualizations of samples marked as *I*, *II*, *III*, and *IV*, are depicted in Figure 3.

Figure 3: Three-dimensional visualizations of sample soil columns and associated measured macropore flow parameters (k_{sat} is saturated permeability, and k_a-100 and D_P/D_0-100 are air permeability and gas diffusivity at -100 cm matric potentials, respectively).

Figure 4: Predictive performance of empirical models for saturated permeability (k_{sat}); filled symbols represent samples with biopore-dominated flow and empty symbols represent samples with matrix-dominated flow; samples marked as *I*, *II*, *III*, and *IV* are depicted in Figure 3.

Figure 5: Predictive performance of empirical models for air permeability (k_a) and gas diffusivity (D_P/D_0) at -30 cm and -100 cm matric potentials. (a) Deepagoda et al. (2011), (b) Deepagoda et al., (2011), (c) WLR-Marshall model (Moldrup et al., 2000), and (d) WLR-Marshall model (Moldrup et al., 2000); filled symbols represent samples with biopore-dominated flow and empty symbols represent samples with matrix-dominated flow; samples marked as *I*, *II*, *III*, and *IV* are depicted in Figure 3.

Figure 6: CT-derived macroporosity plotted as a function of physically measured air-filled porosity at -30 cm matric potential.

Figure 7: Spearman rank order correlation analysis for (a) all samples (N = 65), (b) samples with biopore flow (N = 16), and (c) samples with matrix flow (N = 49); stars indicate

significant correlations at p value < 0.01; where MP is macroporosity, PMP is percolating macroporosity, EPMP is effective percolating macroporosity, MPSSA is macropore specific surface area, MPHR is macropore hydraulic radius, MPMD is macropore mean diameter, MPFD is macropore fractal dimension, MPGC is macropore global connectivity, MPLC is macropore local connectivity, k_{sat} is saturated permeability, k_a-30 is air permeability at -30 cm matric potential, k_a-100 is air permeability at -100 cm matric potential, D_P/D_0-30 is gas diffusivity at -30 cm matric potential, and D_P/D_0-100 is gas diffusivity at -100 cm matric potential, strong correlation (r > 0.70), moderate correlation (r = 0.5 - 0.7), and weak correlation (r < 0.5).

Figure 8: Saturated permeability (k_{sat}), air permeability at -30 cm matric potential (k_a-30), air permeability at -100 cm matric potential (k_a-100), gas diffusivity at -30 cm matric potential (D_P/D_0-30), and gas diffusivity at -100 cm matric potential (D_P/D_0-100) were plotted as a function of selected CT-derived macropore network characteristics; filled symbols represent samples with biopore-dominated flow and empty symbols represent samples with matrix-dominated flow. Either linear or power regressions that best describe data (greater R^2) were fitted if found significant at p < 0.01, two separate regressions were fitted for samples with biopore flow and matrix flow if they were significantly different.

Figure 9: Predictive performance of Ahuja et al. (1984) model using novel input parameters, effective porosity in the original model was replaced with the CT derived total macroporosity (MP) in case of matrix-dominated flow, and with the effective percolating macroporosity (EPMP) in case of biopore-dominated flow, for (a) saturated permeability, (b) air permeability at -30 cm matric potential, (c) air permeability at -100 cm matric potential, (d) gas diffusivity at -30 cm matric potential, and (e) gas diffusivity at -100 cm matric potential.

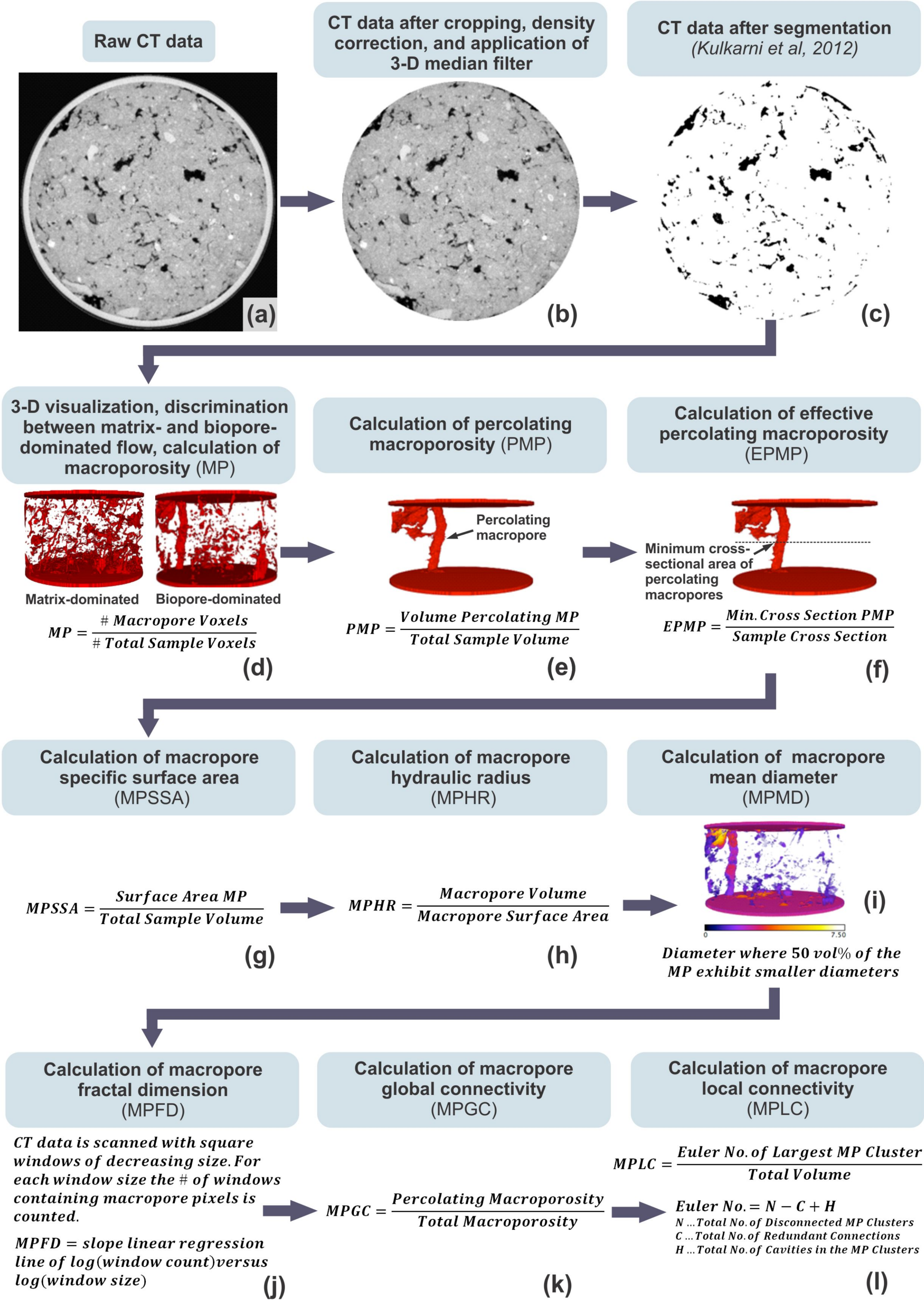

Raw CT data
(a)
CT data after cropping, density correction, and application of 3-D median filter
(b)
CT data after segmentation (Kulkarni et al, 2012)
(c)
3-D visualization, discrimination between matrix- and biopore-dominated flow, calculation of macroporosity (MP)
Matrix-dominated
Biopore-dominated
MP = # Macropore Voxels / # Total Sample Voxels
(d)
Calculation of percolating macroporosity (PMP)
Percolating macropore
PMP = Volume Percolating MP / Total Sample Volume
(e)
Calculation of effective percolating macroporosity (EPMP)
Minimum cross-sectional area of percolating macropores
EPMP = Min. Cross Section PMP / Sample Cross Section
(f)
Calculation of macropore specific surface area (MPSSA)
MPSSA = Surface Area MP / Total Sample Volume
(g)
Calculation of macropore hydraulic radius (MPHR)
MPHR = Macropore Volume / Macropore Surface Area
(h)
Calculation of macropore mean diameter (MPMD)
0
7.50
(i)
Diameter where 50 vol% of the MP exhibit smaller diameters
Calculation of macropore fractal dimension (MPFD)
CT data is scanned with square windows of decreasing size. For each window size the # of windows containing macropore pixels is counted.
MPFD = slope linear regression line of log(window count) versus log(window size)
(j)
Calculation of macropore global connectivity (MPGC)
MPGC = Percolating Macroporosity / Total Macroporosity
(k)
Calculation of macropore local connectivity (MPLC)
MPLC = Euler No. of Largest MP Cluster / Total Volume
Euler No. = N − C + H
N ... Total No. of Disconnected MP Clusters
C ... Total No. of Redundant Connections
H ... Total No. of Cavities in the MP Clusters
(l)

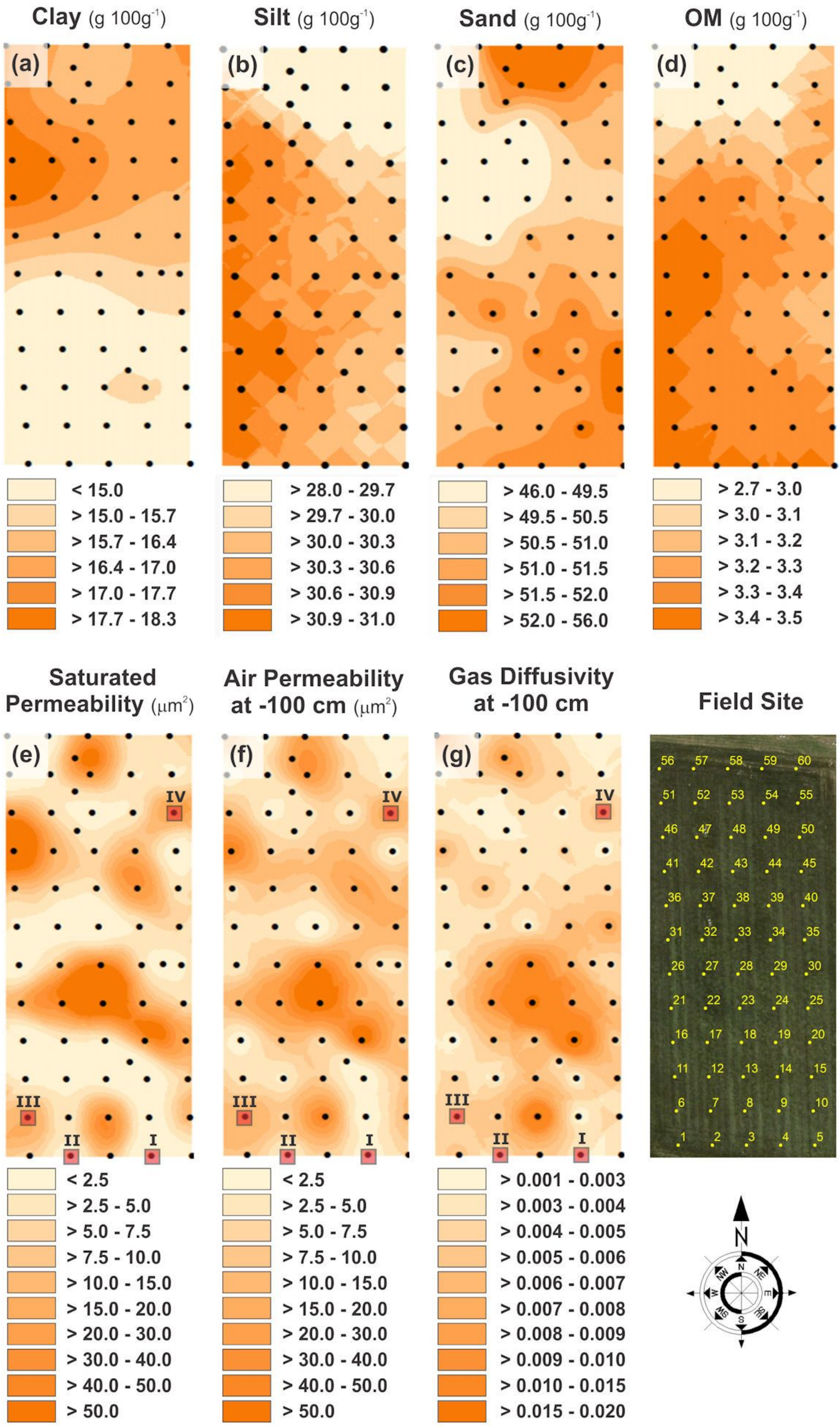

Clay (g 100g-1)
Silt (g 100g-1)
Sand (g 100g-1)
OM (g 100g-1)
(a)
(b)
(c)
(d)
< 15.0
> 15.0 - 15.7
> 15.7 - 16.4
> 16.4 - 17.0
> 17.0 - 17.7
> 17.7 - 18.3
> 28.0 - 29.7
> 29.7 - 30.0
> 30.0 - 30.3
> 30.3 - 30.6
> 30.6 - 30.9
> 30.9 - 31.0
> 46.0 - 49.5
> 49.5 - 50.5
> 50.5 - 51.0
> 51.0 - 51.5
> 51.5 - 52.0
> 52.0 - 56.0
> 2.7 - 3.0
> 3.0 - 3.1
> 3.1 - 3.2
> 3.2 - 3.3
> 3.3 - 3.4
> 3.4 - 3.5
Saturated Permeability (μm2)
Air Permeability at -100 cm (μm2)
Gas Diffusivity at -100 cm
Field Site
(e)
(f)
(g)
IV
III
II
I
< 2.5
> 2.5 - 5.0
> 5.0 - 7.5
> 7.5 - 10.0
> 10.0 - 15.0
> 15.0 - 20.0
> 20.0 - 30.0
> 30.0 - 40.0
> 40.0 - 50.0
> 50.0
> 0.001 - 0.003
> 0.003 - 0.004
> 0.004 - 0.005
> 0.005 - 0.006
> 0.006 - 0.007
> 0.007 - 0.008
> 0.008 - 0.009
> 0.009 - 0.010
> 0.010 - 0.015
> 0.015 - 0.020
56 57 58 59 60
51 52 53 54 55
46 47 48 49 50
41 42 43 44 45
36 37 38 39 40
31 32 33 34 35
26 27 28 29 30
21 22 23 24 25
16 17 18 19 20
11 12 13 14 15
6 7 8 9 10
1 2 3 4 5
N

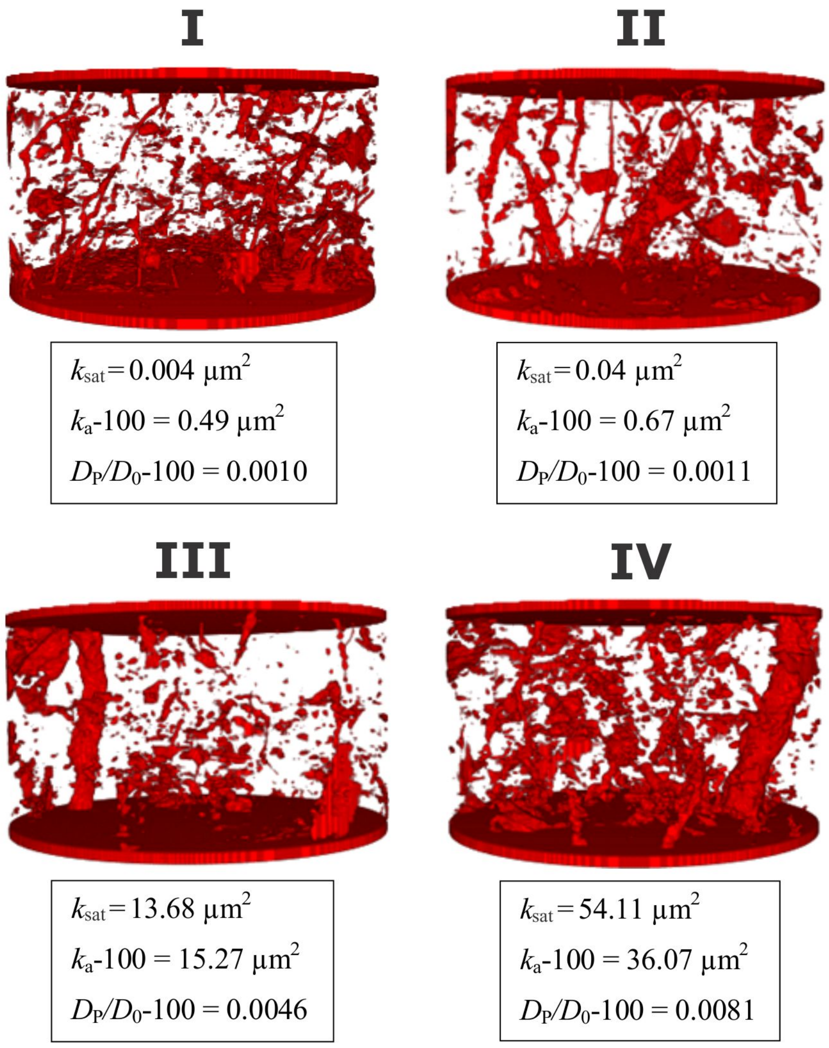
I
k_{sat} = 0.004 μm^2
k_a-100 = 0.49 μm^2
D_P/D_0-100 = 0.0010
II
k_{sat} = 0.04 μm^2
k_a-100 = 0.67 μm^2
D_P/D_0-100 = 0.0011
III
k_{sat} = 13.68 μm^2
k_a-100 = 15.27 μm^2
D_P/D_0-100 = 0.0046
IV
k_{sat} = 54.11 μm^2
k_a-100 = 36.07 μm^2
D_P/D_0-100 = 0.0081

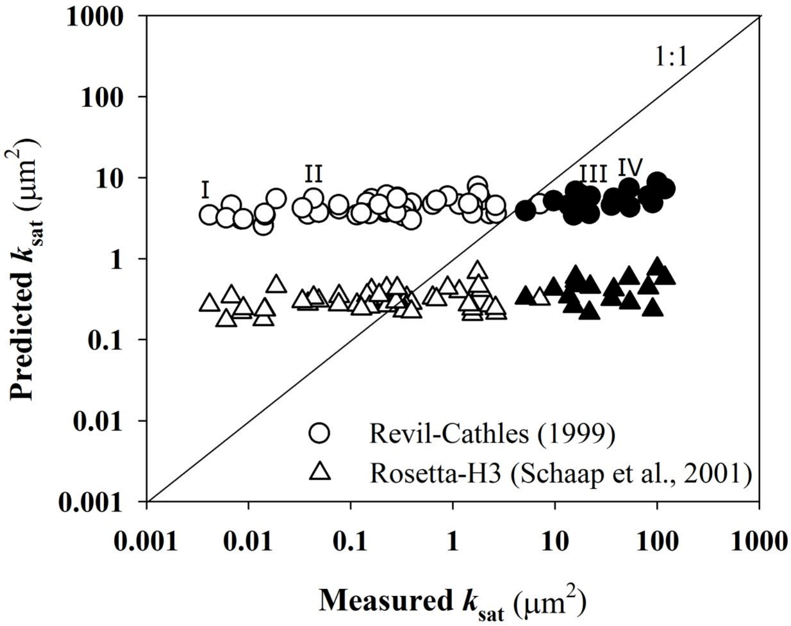

1000
100
10
1
0.1
0.01
0.001
Predicted k_{sat} (μm^2)
1:1
I
II
III
IV
Revil-Cathles (1999)
Rosetta-H3 (Schaap et al., 2001)
0.001
0.01
0.1
1
10
100
1000
Measured k_{sat} (μm^2)

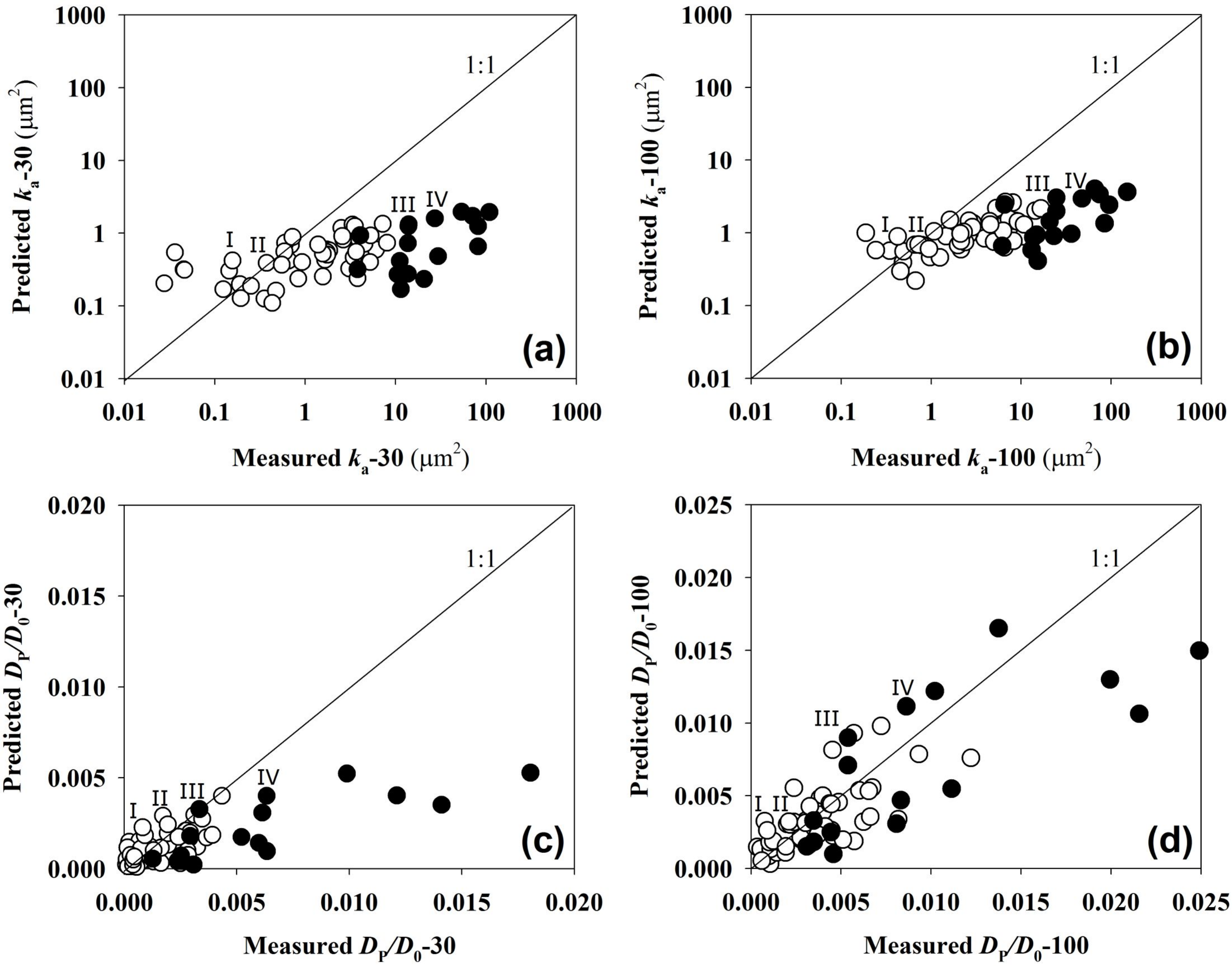

Predicted k_a-30 (μm^2)
Measured k_a-30 (μm^2)
1:1
I
II
III
IV
(a)
1000
100
10
1
0.1
0.01
0.01
0.1
1
10
100
1000
Predicted k_a-100 (μm^2)
Measured k_a-100 (μm^2)
1:1
I
II
III
IV
(b)
Predicted D_P/D_0-30
Measured D_P/D_0-30
1:1
I
II
III
IV
(c)
0.000
0.005
0.010
0.015
0.020
Predicted D_P/D_0-100
Measured D_P/D_0-100
1:1
I
II
III
IV
(d)
0.000
0.005
0.010
0.015
0.020
0.025

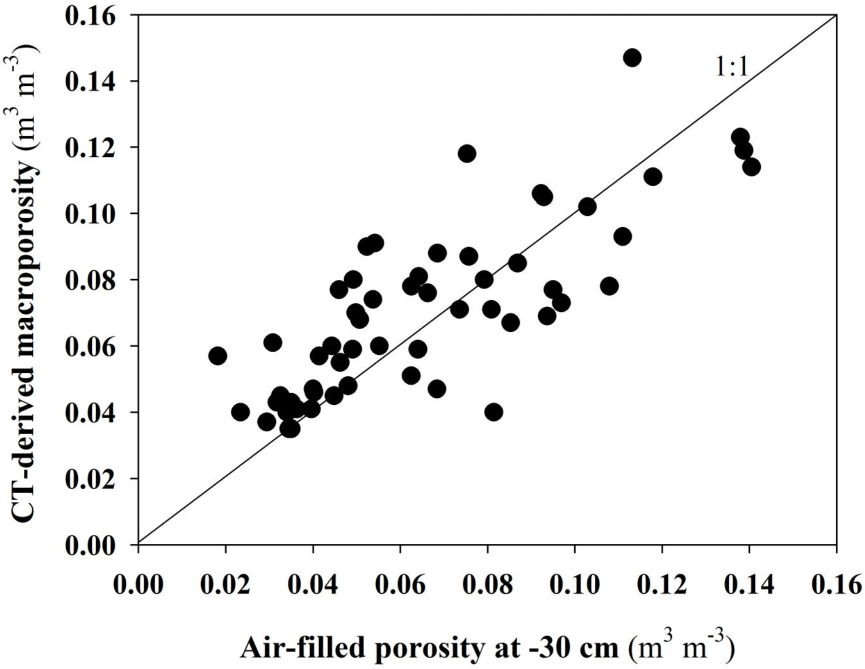

1:1
CT-derived macroporosity (m3 m-3)
0.00
0.02
0.04
0.06
0.08
0.10
0.12
0.14
0.16
Air-filled porosity at -30 cm (m3 m-3)

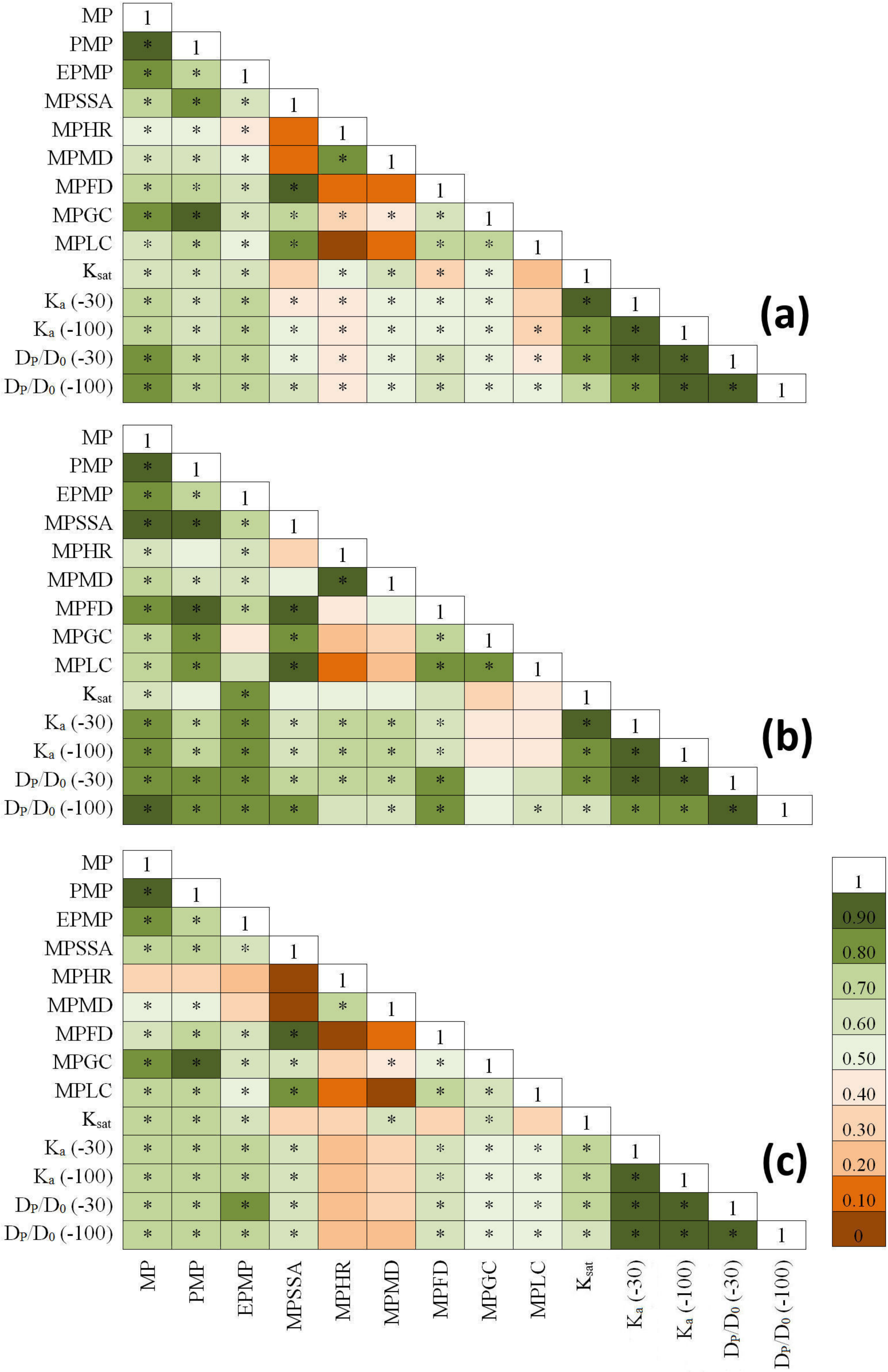
MP
PMP
EPMP
MPSSA
MPHR
MPMD
MPFD
MPGC
MPLC
Ksat
Ka (-30)
Ka (-100)
DP/D0 (-30)
DP/D0 (-100)
(a)
(b)
(c)
1
0.90
0.80
0.70
0.60
0.50
0.40
0.30
0.20
0.10
0

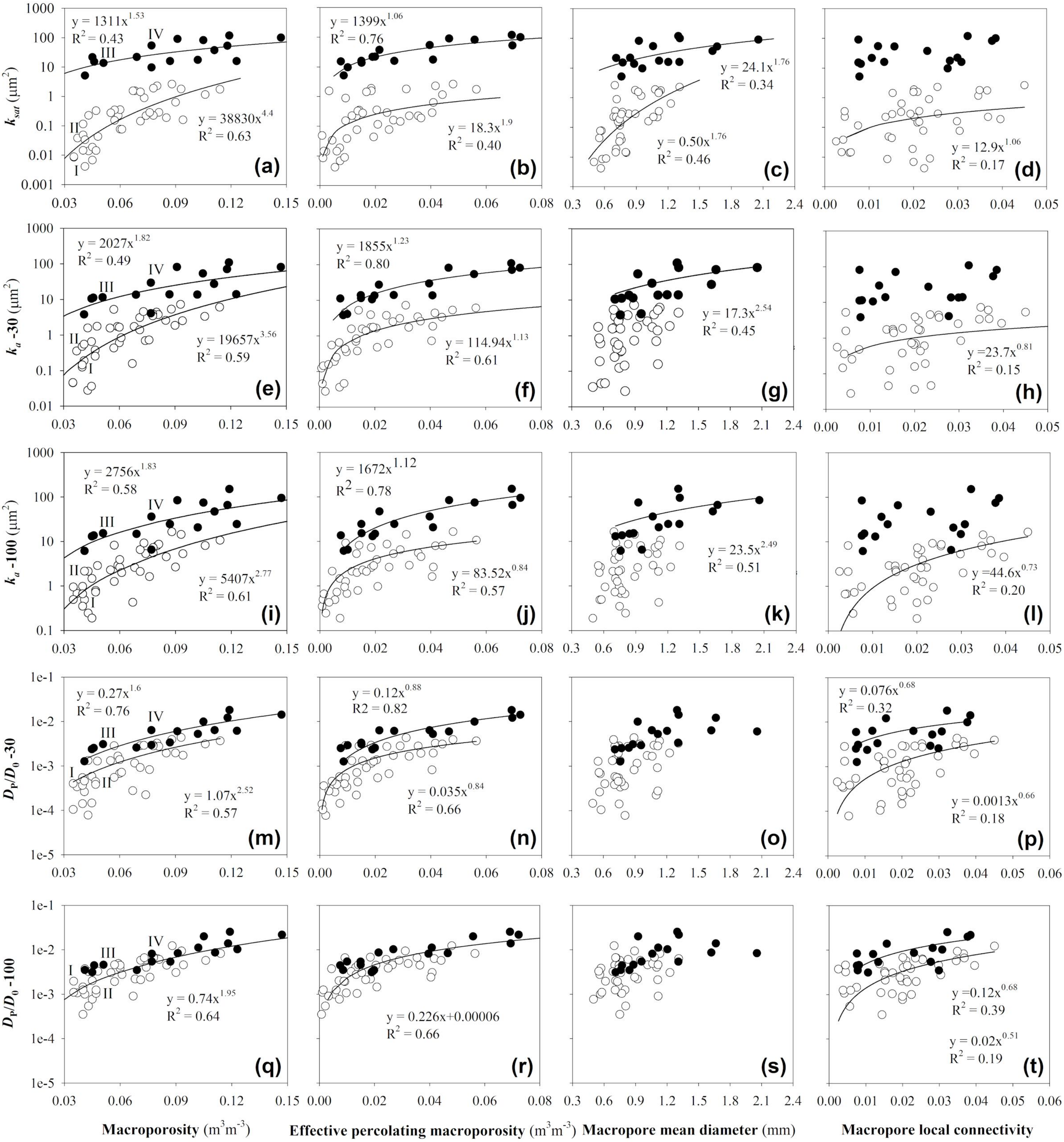

y = 1311x^1.53
R^2 = 0.43
y = 38830x^4.4
R^2 = 0.63
(a)
y = 1399x^1.06
R^2 = 0.76
y = 18.3x^1.9
R^2 = 0.40
(b)
y = 24.1x^1.76
R^2 = 0.34
y = 0.50x^1.76
R^2 = 0.46
(c)
y = 12.9x^1.06
R^2 = 0.17
(d)
y = 2027x^1.82
R^2 = 0.49
y = 19657x^3.56
R^2 = 0.59
(e)
y = 1855x^1.23
R^2 = 0.80
y = 114.94x^1.13
R^2 = 0.61
(f)
y = 17.3x^2.54
R^2 = 0.45
(g)
y =23.7x^0.81
R^2 = 0.15
(h)
y = 2756x^1.83
R^2 = 0.58
y = 5407x^2.77
R^2 = 0.61
(i)
y = 1672x^1.12
R^2 = 0.78
y = 83.52x^0.84
R^2 = 0.57
(j)
y = 23.5x^2.49
R^2 = 0.51
(k)
y =44.6x^0.73
R^2 = 0.20
(l)
y = 0.27x^1.6
R^2 = 0.76
y = 1.07x^2.52
R^2 = 0.57
(m)
y = 0.12x^0.88
R2 = 0.82
y = 0.035x^0.84
R^2 = 0.66
(n)
(o)
y = 0.076x^0.68
R^2 = 0.32
y = 0.0013x^0.66
R^2 = 0.18
(p)
y = 0.74x^1.95
R^2 = 0.64
(q)
y = 0.226x+0.00006
R^2 = 0.66
(r)
(s)
y = 0.12x^0.68
R^2 = 0.39
y = 0.02x^0.51
R^2 = 0.19
(t)
I
II
III
IV
k_sat (μm^2)
k_a -30 (μm^2)
k_a -100 (μm^2)
D_P/D_0 -30
D_P/D_0 -100
Macroporosity (m^3m^-3)
Effective percolating macroporosity (m^3m^-3)
Macropore mean diameter (mm)
Macropore local connectivity

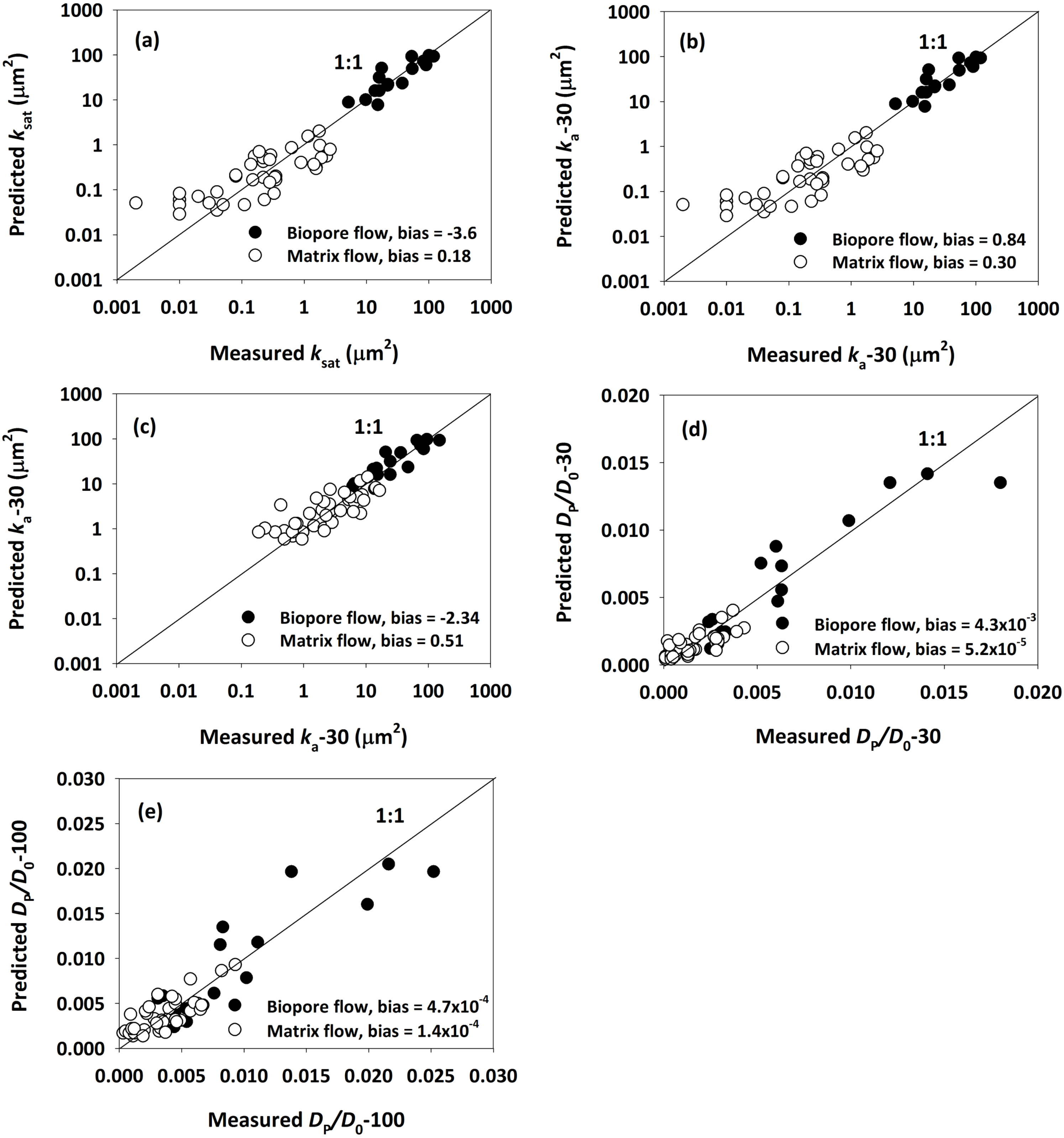

(a)
1:1
Predicted k_{sat} (μm^2)
Measured k_{sat} (μm^2)
Biopore flow, bias = -3.6
Matrix flow, bias = 0.18
(b)
1:1
Predicted k_a-30 (μm^2)
Measured k_a-30 (μm^2)
Biopore flow, bias = 0.84
Matrix flow, bias = 0.30
(c)
1:1
Predicted k_a-30 (μm^2)
Measured k_a-30 (μm^2)
Biopore flow, bias = -2.34
Matrix flow, bias = 0.51
(d)
1:1
Predicted D_P/D_0-30
Measured D_P/D_0-30
Biopore flow, bias = 4.3x10^{-3}
Matrix flow, bias = 5.2x10^{-5}
(e)
1:1
Predicted D_P/D_0-100
Measured D_P/D_0-100
Biopore flow, bias = 4.7x10^{-4}
Matrix flow, bias = 1.4x10^{-4}